








Crystallographic and magnetic structures of the VI_3 and LiVI_3 van der Waals compounds

Thomas Marchandier ¹, Nicolas Dubouis ¹, François Fauth ², Maxim Avdeev ³, Alexis Grimaud ¹,
Jean-Marie Tarascon ¹ and Gwenaëlle Rousse ^{1,*}

¹Collège de France, Chaire de Chimie du Solide et de l'Énergie, UMR 8260, 11 place Marcelin Berthelot, 75231 Paris Cedex 05, France;
Réseau sur le Stockage Electrochimique de l'Énergie (RS2E), FR CNRS 3459, 75005 Paris, France;
and Sorbonne Université, 4 place Jussieu, F-75005 Paris, France

²CELLS -ALBA synchrotron, Cerdanyola del Valles, Barcelona E-08290, Spain

³School of Chemistry, the University of Sydney, Sydney NSW 2006, Australia
and Australian Centre for Neutron Scattering, Australian Nuclear Science and Technology Organisation, New Illawarra Rd,
Lucas Heights NSW 2234, Australia



(Received 2 April 2021; revised 14 June 2021; accepted 21 June 2021; published 12 July 2021)

Two-dimensional (2D) layered magnetic materials are generating a great amount of interest for the next generation of electronic devices thanks to their remarkable properties associated with spin dynamics. The recently discovered layered VI_3 ferromagnetic phase belongs to this family, although a full understanding of its properties is limited by the incomplete understanding of its crystallographic structure. The motivation of this work is to address this issue. Here, we investigate the VI_3 crystal structures at low temperature using both synchrotron x-ray and neutron powder diffraction and provide structural models for the two structural transitions occurring at 76 and 32 K. Moreover, we confirm by magnetic measurements that VI_3 becomes ferromagnetic at 50 K and we question the establishment of a long-range magnetic structure by neutron diffraction. We equally determined the magnetic properties of our recently reported LiVI_3 phase, which is like the well-known CrI_3 ferromagnetic phase in terms of electronic and crystallographic structures and found an antiferromagnetic behavior with a Néel temperature of 12 K. Such a finding provides extra clues for a better understanding of magnetism in these low-dimension compounds. Finally, the easiness of preparing Li-based 2D magnetic materials by chemical/electrochemical means opens wide the opportunity to design materials with exotic properties.

DOI: [10.1103/PhysRevB.104.014105](https://doi.org/10.1103/PhysRevB.104.014105)

I. INTRODUCTION

Two-dimensional (2D) materials such as graphene are among the most promising candidates to enhance electronic devices while enabling future upcoming technologies, hence the great attention that they are capturing in the scientific community [1]. Moreover, fundamentally, they offer a fascinating playground for physicists owing to the complexity of their spin dynamics involving ferromagnetic and antiferromagnetic resonances [2]. For instance, although in an ideal magnetically isotropic 2D material long-range magnetic order is impossible due to the Mermin-Wagner theorem [2], the discovery of ferromagnetic order in two-dimensional materials such as $\text{Cr}_2\text{Ge}_2\text{Te}_6$ [3] or CrI_3 [4] opened new horizons to investigate spintronic systems. Thus, the discovery of new ferromagnetic-layered van der Waals (vdW) materials is of prime importance as illustrated by the recent discovery of ferromagnetic order in the layered semiconductor VI_3 [5].

VI_3 presents a Curie temperature slightly lower than the widely studied CrI_3 (50 K vs 60 K) but a different electronic structure (d^2 vs d^3). The two compounds VI_3 and CrI_3 provide

a unique opportunity to understand the implication of the electronic structure on their magnetic properties. However, this could not happen yet because the crystal structure is still the subject of intense debates and the source of contradictory reports [5–7] for the room-temperature structure. Moreover, upon cooling, VI_3 undergoes two successive phase transitions at around 76 K [5,7] and 32 K [8] whose crystallographic structures have not been fully determined yet. Additionally, experimental and theoretical investigations suggest an unusual magnetic behavior at low temperature, with one or several ferromagnetic transitions [9].

In this paper, we investigate both the crystal and magnetic structures of VI_3 from room temperature (RT) down to 3 K using high-angular resolution synchrotron x-ray powder diffraction (SXRD) and neutron powder diffraction. In particular, we confirm the $R\bar{3}$ structural model at room temperature and the presence of two structural transitions at low temperature around 76 and 32 K. We propose here structural models for the low-temperature phases of VI_3 and discuss its magnetic structure with the help of both low-temperature neutron diffraction and magnetization measurements. In parallel, we measured the magnetic behavior of the layered LiVI_3 phase, recently synthesized by our group via chemical insertion of Li in VI_3 [10] and found an antiferromagnetic behavior as compared to the ferromagnetic behavior reported for CrI_3 [3],

*gwenaelle.rousse@sorbonne-universite.fr

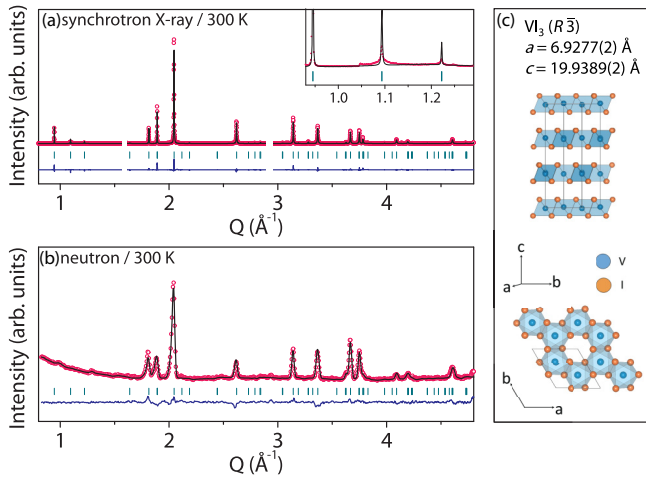


FIG. 1. Synchrotron x-ray (a) and neutron (b) Rietveld refinements of VI_3 at 300 K. Wavelengths for synchrotron x rays and neutrons are $\lambda = 0.3869 \text{ \AA}$ and $\lambda = 2.4184 \text{ \AA}$, respectively. The pink circles, black continuous line, and bottom blue line represent the observed, calculated, and difference patterns, respectively. Vertical green tick bars stand for the Bragg positions. Two regions were excluded due to a minute amount of impurities. The inset in (a) highlights the indexation of the superstructure peaks. (c) Structure of VI_3 at 300 K.

although both compounds are alike in terms of structural and electronic configurations.

II. RESULTS AND DISCUSSION

A. Experimental procedures

Pure VI_3 powders were obtained through iodine vapor transport in quartz tubes under high vacuum as already described elsewhere [5]. Vanadium metal powder (Alfa Aesar, 99.9%) was mixed with a slight excess of iodine (1:1.1 molar ratio) inside an argon filled glove box; the mixture was then poured in a quartz tube subsequently sealed under high vacuum (10^{-6} bar). The tube was placed in a tubular furnace in such a way that one end of the tube was at room temperature whereas the other one was positioned in the middle of the furnace and heated at $450 \text{ }^\circ\text{C}$ for 72 h. After reaction, the tube was opened inside a glove box and the powder was placed in a Schlenk flask and purified under dynamic vacuum at $200 \text{ }^\circ\text{C}$. LiVI_3 powder was prepared by stirring VI_3 powder in an excess (1:3 molar ratio) of *n*-butyl lithium (2.5 M in hexane, Sigma-Aldrich) under argon atmosphere. After a 1-h reaction, the suspension was centrifuged and rinsed three times with hexane before being dried under dynamic vacuum.

Synchrotron x-ray powder diffraction (SXRD) patterns were collected on the BL04-MSPD beamline of the ALBA synchrotron (Barcelona area) using the multianalyzer detection (MAD) setup offering the highest possible instrumental angular resolution, $\Delta(2\theta) < 0.006^\circ$ in the 0° – 35° 2θ range [11,12]. Powders were sealed in Ar glove box in a 0.6 mm diameter borosilicate capillary and transferred to a Dynaflo liquid helium flow cryostat [13]. SXRD experiments were performed at 32 keV energy, slightly below the iodine *K* edge to minimize absorption. The exact wavelength ($\lambda = 0.38692 \text{ \AA}$)

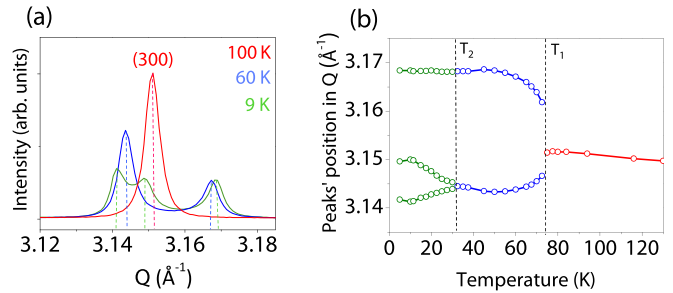


FIG. 2. Evolution of selected reflections with temperature: (a) evolution of the (300) peak (indices refer to the $R\bar{3}$ cell); (b) evolution of the peaks' positions.

was determined from the first six Bragg reflections of a NIST silicon standard SRM 640e.

Constant wavelength neutron powder diffraction (NPD) data were collected on the ECHIDNA high-resolution and WOMBAT high-intensity neutron powder diffractometers [14,15] using the wavelengths of 2.4395 and 2.4184 \AA , respectively. For VI_3 , the NPD data were collected on ECHIDNA at 9, 40, 60, and 90 K and on WOMBAT every 1 K in the range 3–92 K. For LiVI_3 , the NPD data were collected only on ECHIDNA at 3 and 25 K. To prevent reaction of the samples with ambient atmosphere, the samples were loaded into 9 mm diameter cylindrical vanadium cans in an Ar glove box and sealed with an indium wire.

Finally, all the SXRD diffraction patterns were refined using the Rietveld method with the FULLPROF program [16].

The evolution of the magnetic susceptibility with temperature was measured using a superconducting quantum interference device (SQUID) (XL, Quantum Design), under zero field cooled (ZFC) conditions between 2 and 400 K with an applied magnetic field of 10 kOe. Magnetization curves were recorded at 2 K varying magnetic field in a [–70 kOe; 70 kOe] range.

B. Crystal structure of VI_3 from RT to 9 K

1. Room-temperature structure

VI_3 have long been reported to adopt a BiI_3 -type structure [17] analogous to VCl_3 and VBr_3 with the $R\bar{3}$ space group, but recent publications have challenged this assignment with reports of alternative $P\bar{3}1c$ [7] or $C2/m$ [6] space groups. These different models commonly agree that VI_6 octahedra share edges to form layers into which vanadium atoms fill two-thirds of the octahedral positions to form a honeycomb pattern. These honeycomb layers are then stacked one above the other, and layers are separated by a van der Waals gap. Their discrepancies are nested in the different stacking sequences of the VI_3 layers along the *c* axis. For instance, the $C2/m$ model proposed by Tian *et al.* [6] implies an ABC stacking of the iodine atoms in opposition to an ABAB one for both the $R\bar{3}$ and the $P\bar{3}1c$ models. The difference between the two latter models is more subtle and originates from different honeycomb stackings, which result in only minute variations in the x-ray powder diffraction patterns. In order to clarify the VI_3 room-temperature structure, we tried to refine the experimental synchrotron powder pattern collected at room

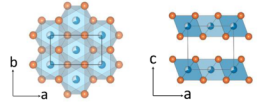
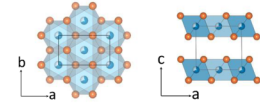
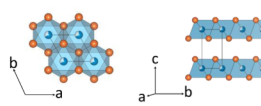
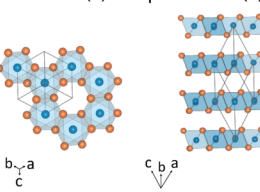
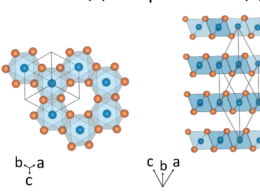
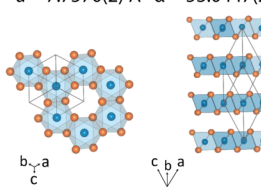
	9 K	60 K	300 K
Average model (without superstructure)	$P\bar{1}$ $a = 6.9353(2) \text{ \AA}$ $\alpha = 90.1044(6)^\circ$ $b = 3.9655(2) \text{ \AA}$ $\beta = 90.3956(5)^\circ$ $c = 6.5910(2) \text{ \AA}$ $\gamma = 90.1495(5)^\circ$ 	$C2/m$ $a = 6.9395(2) \text{ \AA}$ $\beta = 90.4539(4)^\circ$ $b = 3.9671(2) \text{ \AA}$ $c = 6.5960(2) \text{ \AA}$ 	$P\bar{3}m1$ (Hexagonal cell) $a = 3.9998(2) \text{ \AA}$ $c = 6.6462(2) \text{ \AA}$ 
Complete model (with superstructure)	$P\bar{1}$ $a = 7.7268(2) \text{ \AA}$ $\alpha = 53.1280(2)^\circ$ $b = 7.6808(2) \text{ \AA}$ $\beta = 53.0863(3)^\circ$ $c = 7.6985(2) \text{ \AA}$ $\gamma = 53.5022(3)^\circ$ 	$P\bar{1}$ $a = 7.7359(2) \text{ \AA}$ $\alpha = 53.1933(5)^\circ$ $b = 7.6886(2) \text{ \AA}$ $\beta = 53.0168(7)^\circ$ $c = 7.6968(2) \text{ \AA}$ $\gamma = 53.4732(7)^\circ$ 	$R\bar{3}$ (Hexagonal cell) $a = 6.9277(2) \text{ \AA}$ $c = 19.9389(2) \text{ \AA}$ $R\bar{3}$ (Rhombohedral cell) $a = 7.7570(2) \text{ \AA}$ $\alpha = 53.0447(2)^\circ$ 

FIG. 3. Overview of the different structural models at 9, 60, and 300 K. The upper row presents the “average models” where the honeycomb superstructure is not taken into account. The lower row presents the “complete models” including the vanadium superstructure.

temperature with those different models (cf. Fig. S1 in the Supplemental Material (SM) [18]). While the $C2/m$ model (ABC stacking of iodine layers) is clearly inadequate to index our pattern, the other models (ABAB stacking of iodine layers) led to decent fits, and solely the indexing of small low-angle reflections specific to the vanadium honeycomb superstructure allowed discriminating them. The only space group able to index all these peaks was $R\bar{3}$, with lattice parameters $a = 6.9277(2) \text{ \AA}$, $c = 19.9389(2) \text{ \AA}$, and this model led to the best refinement (Figs. 1(a) and 1(b) and Table S1 [18]). In this structure, the iodine layers are stacked in an ABAB manner (O1 type) whereas the vanadium honeycomb motifs adopt an ABC sequence. This structural model assignment from powder diffraction is supported by single-crystal diffraction [5], where the differences between these trigonal space groups are easier to spot, provided that good quality single crystals are available.

It is worth mentioning that a good refinement can also be obtained in a ninefold smaller unit cell with $a = 3.9998(2) \text{ \AA}$, $c = 6.6462(2) \text{ \AA}$ ($P\bar{3}m1$ space group) (cf. Fig. S1 and Table S2 [18]). This cell indexes all peaks, except the superstructure ones associated with the honeycomb ordering, and corresponds to a structural model in which vanadium sits in a $1a$ Wyckoff site with a two-thirds occupancy. For the rest of the paper this model will be referred to as “the average model” as opposed to the “complete model” taking into account the vanadium honeycomb ordering. Considering the lattice centering translations in $R\bar{3}$, the complete model is therefore a threefold superstructure of the average model.

2. Low-temperature structures

The structural evolution of VI_3 upon cooling was explored by high-angular resolution synchrotron x-ray powder diffraction. From RT to 80 K the structure described above is preserved with, however, a contraction of the lattice parameters. When lowering the temperature further, the SXRD

patterns show a first abrupt splitting of peaks (cf. Fig. 2) at 76 K and a second one, less drastic, at temperatures around 32 K. Such features are in agreement with the reported first- and second-order phase transitions at $T_1 \approx 76 \text{ K}$ [5–8] and $T_2 = 32 \text{ K}$ [8], respectively. Nevertheless no structural models have been proposed for the lowest-temperature phase. For the intermediate phase, the only model reported in the literature [7] was deduced from an x-ray powder pattern showing a strong preferred orientation, and whose RT analog was refined in $P\bar{3}1c$, a space group we excluded as discussed earlier. Thus, we embarked on solving the structure of these two low-temperature phases using high-angular resolution SXRD. Diffraction patterns were collected at 60 and 9 K in Debye-Scherrer geometry (powder filled in glass capillaries) to avoid preferred orientation effects. In a first approach, the structures were solved without considering the vanadium honeycomb superstructure (average models), and the second time a more complex but realistic structural description was built by adding the honeycomb vanadium superstructure to the average model (complete models).

Average model. The 60 K SXRD pattern (excluding the superstructure peaks) can be indexed in a monoclinic unit cell with $a = 6.9395(2) \text{ \AA}$, $b = 3.9671(2) \text{ \AA}$, $c = 6.5960(2) \text{ \AA}$, $\beta = 90.4539(4)^\circ$, that is related to the RT average cell using the following transformation:

$$(a_m \quad b_m \quad c_m) = (a_h \quad b_h \quad c_h) \begin{pmatrix} 2 & 0 & 0 \\ 1 & 1 & 0 \\ 0 & 0 & 1 \end{pmatrix}.$$

where the m and h subscripts stand for monoclinic and hexagonal ($P\bar{3}m1$ space group) cells, respectively. It is worth mentioning that this transformation is the one commonly used to relate the trigonal/hexagonal cell to the C -centered orthorhombic cell; therefore the distortion from room temperature to 60 K corresponds solely to a change of the orthorhombic β angle from 90° (RT) to $\beta = 90.4539(4)^\circ$ (60 K).

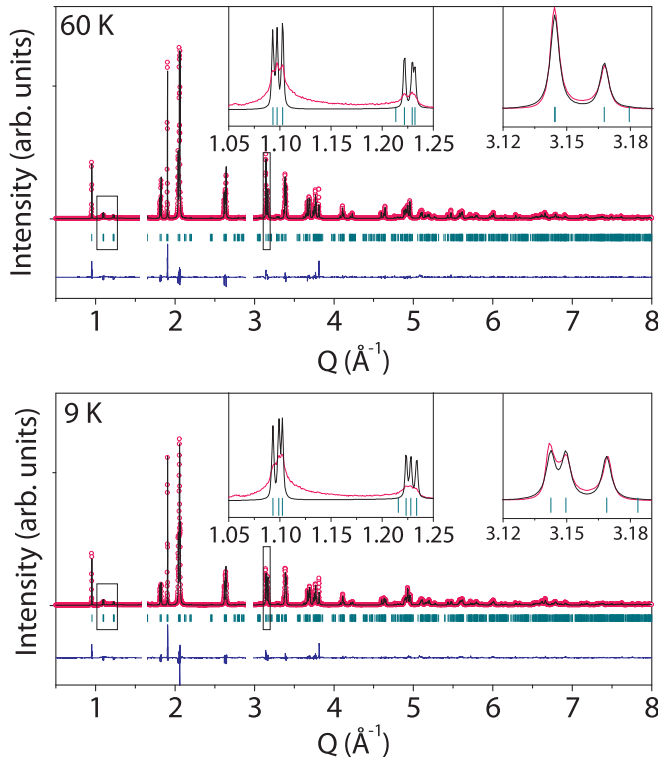


FIG. 4. Synchrotron XRD Rietveld refinement of VI_3 at 60 K (top) and 9 K (bottom) using the “complete model” in the $P\bar{1}$ space group reported in Tables S5 and S6 in the Supplemental Material [18]. Wavelength for the synchrotron x ray is $\lambda = 0.3869 \text{ \AA}$. The pink circles, black continuous line, and bottom blue line represent the observed, calculated, and difference patterns, respectively. Vertical green tick bars stand for the Bragg positions. Some regions were excluded due to a minute amount of impurities. The insets in each figure refer to a zoom of the angular regions shown by a black rectangle in the main figure. The middle inset highlights the indexing of the superstructure peaks whereas the right one highlights the Q range represented in Fig. 2(a).

Then, the pattern was refined via the Rietveld method using the space group $C2/m$ confirming the plausibility of the model (cf. Fig. S3 and Table S3 in the SM [18]). At 9 K, the symmetry was further lowered to the $P\bar{1}$ space group without changing the unit cell metrics and the model was refined against the SXRD pattern (cf. Fig. S3 and Table S4 [18]). A decent fit of the SXRD pattern, which gave a satisfactory representation of the structure, was obtained with the average model. However, although contributing only to a limited extent to the diffraction pattern intensity, the superstructure peaks are of prime importance to understand the physical properties of the material and have to be considered.

Complete model. Assuming that the vanadium superstructure observed at RT (honeycomb layers stacked in an ABC sequence) is preserved in the low-temperature phases, a supercell was built from the average model (cf. SM Sect. 2b for details) with the following transformation:

$$(a_s \quad b_s \quad c_s) = (a_a \quad b_a \quad c_a) \begin{pmatrix} -1/2 & 1/2 & 0 \\ 1/2 & 1/2 & -1 \\ 1 & 1 & 1 \end{pmatrix}.$$

Here the s and a subscripts stand for supercell and average cell, respectively. At room temperature, this supercell represented in Fig. 3 corresponds to the rhombohedral cell of the $R\bar{3}$ model ($a = b = c = 7.7570(2) \text{ \AA}$ and $\alpha = \beta = \gamma = 53.0447(2)^\circ$; see SM Table S1 [18]).

Then, Rietveld refinements of the 60 and 9 K patterns using this model led to a good indexing of the superstructure peaks’ splitting observed on cooling (cf. Fig. 4 and Tables S5 and S6 [18]). The visible shape mismatch between the calculated and the measured superstructure peaks likely accounts for the presence of stacking faults, as commonly encountered in such layered materials [19], and strain developing across the phase transitions. Finally, this two-step refinement process enabled the derivation of the atomic positions and lattice parameters from the average model which prevented our refinements from diverging with such a large number of refined parameters. All complete and average structural models for VI_3 are summarized in Fig. 5 together with the corresponding transformation matrices.

To further understand the origin of the observed distortions we represent in Fig. 6 the evolution of the V-V distances in the honeycomb layers. Above 76 K, vanadium atoms describe regular hexagons in the layers. In contrast, below this temperature, a contraction of one of the V-V distances leads to the formation of vanadium dimers. This finding contradicts the vanadium antidimerization deduced by Son *et al.* [7]. Finally, below 32 K, the honeycomb framework is further distorted, leading to three distinct V-V distances inside the layer. Similar behaviors have been reported for other transition metal trichlorides $M\text{Cl}_3$ (namely, TiCl_3 , MoCl_3 , or TcCl_3), with, however, a larger difference between long and short $M\text{-Cl}$ distances [20].

At this stage, it is important to consider the connection between those complex structural transitions and the onset of ferromagnetic order at $T_C = 50 \text{ K}$ in VI_3 that we confirm in our homemade sample (cf. the following section). Obviously, the 76 K structural phase transition that occurs far above T_C (50 K) is free of magnetic effects. Between T_1 (76 K) and T_2 (32 K), it is worth noting that the evolution of the lattice parameters and characteristic distances in the VI_3 structure are not monotonous (cf. Fig. 7). More specifically, we observe that the V-V and interlayer (van der Waals) distances [cf. Figs. 7(a) and 7(b)] increase from 76 to 50 K while they decrease upon further cooling. This anomaly is directly linked to the establishment of a magnetic order in the structure and is strongly indicative of a magnetostriction phenomenon already suggested by Doležal *et al.* [8]. Finally, the origin of the low-temperature structural phase transition at $T_2 = 32 \text{ K}$ still remains to be explained in conjunction with the magnetic ordering at 50 K.

To interrogate the presence of a long-range magnetic ordering in VI_3 , we collected neutron diffraction patterns between 3 and 100 K. The patterns are reported in Fig. 8(a) and confirm the occurrence of structural phase transitions at $T_1 = 76 \text{ K}$ and $T_2 = 32 \text{ K}$, previously spotted by x-rays. The latter is, however, barely observable because of the lower resolution of the neutron diffractometer compared to the synchrotron XRD one. The magnetic signature related to the ferromagnetic ordering is even more difficult to observe. Nevertheless some hints can be spotted by comparing

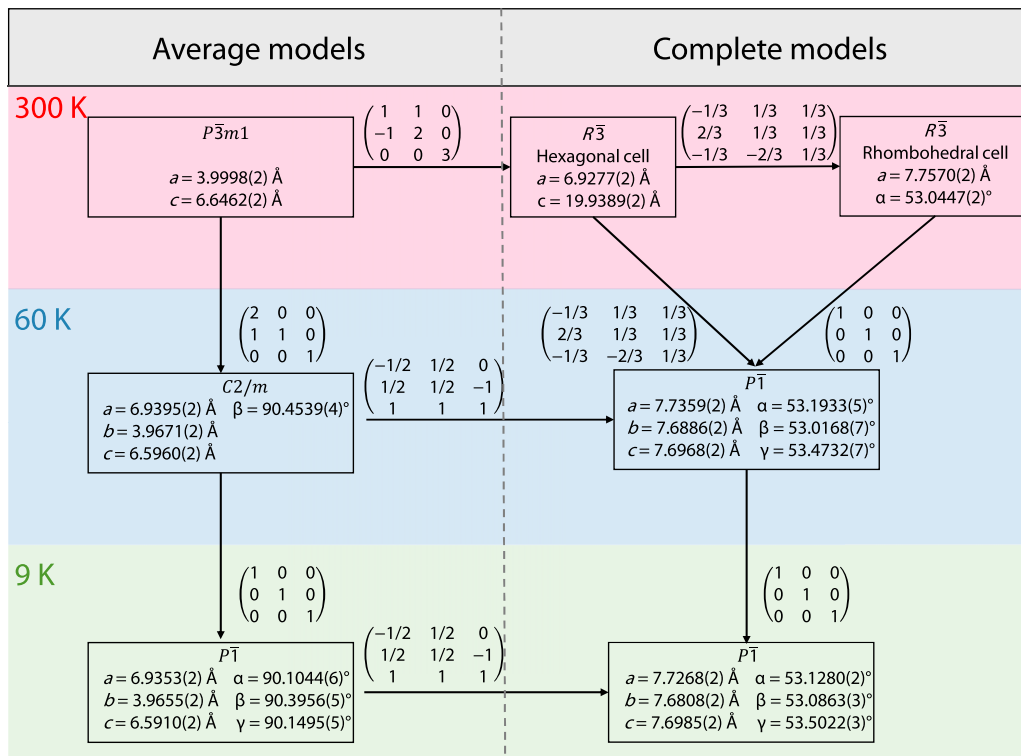


FIG. 5. Summary of the different structural models of VI_3 and the associated transformation matrices.

the 60 K (above T_c), and 40 and 9 K (both below T_c) patterns. They show a subtle intensity evolution of the (110) peak [at $Q = 1.84 \text{ \AA}^{-1}$, here (hkl) indices refer to the $R\bar{3}$

hexagonal cell] [cf. Figs. 8(c) and 8(d)] with no further visible evolution of this peak's intensity down to the lowest measured temperature. An increase of the (110) peaks is expected with a ferromagnetic order with magnetic moments oriented perpendicular to the honeycomb vanadium layers (along [001]) [cf. Fig. 8(b)], as deduced from simulations of ferromagnetic contributions along different directions (cf. SM Part 3, Fig. S6 [18]). However, if of magnetic origin, this subtle intensity increase would correspond to an ordered

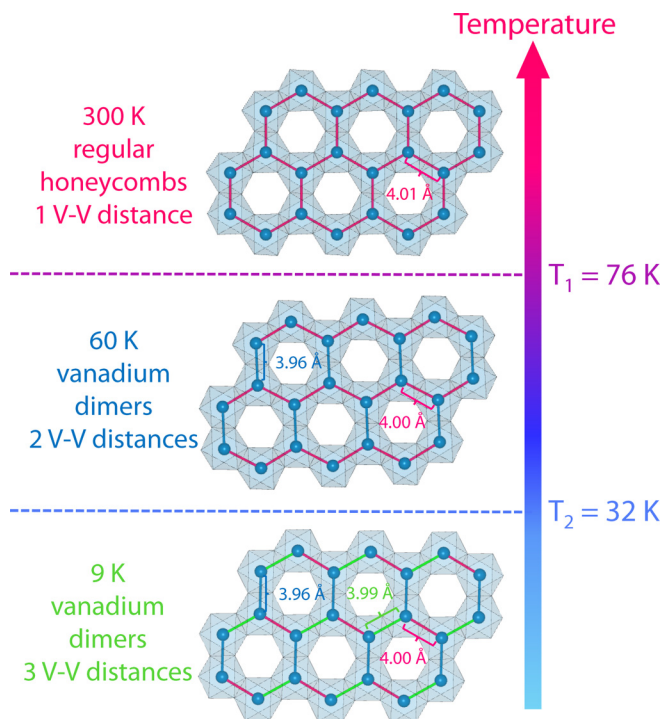


FIG. 6. Evolution of the V-V distances in the honeycomb motifs at 300, 60, and 9 K, deduced from the complete structural models reported in Tables S1, S5, and S6 in the Supplemental Material [18].

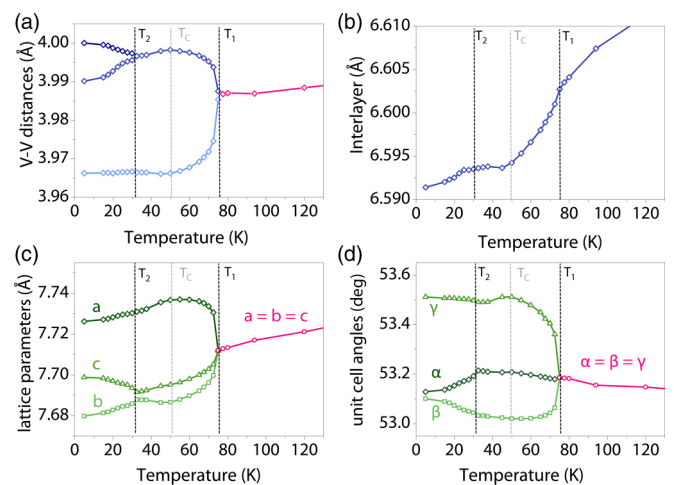


FIG. 7. Evolution of (a) the vanadium-vanadium distances, (b) the interlayer distance (defined as the distance between two vanadium layers) and (c,d) lattice parameters of VI_3 from 10 to 140 K. These parameters are given using the complete model settings described in Fig. 3, and the high-temperature phase is described in the rhombohedral primitive cell of $R\bar{3}$.

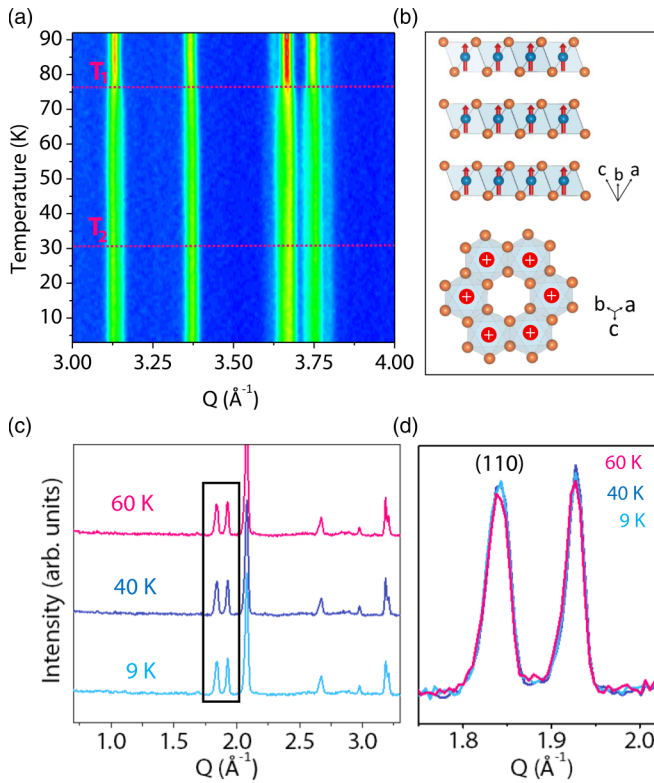


FIG. 8. (a) Evolution of the neutron diffraction patterns with temperature between 3 and 92 K. It is worth noticing that the neutron instrument resolution is not high enough to clearly distinguish the structural transition at T_2 . (b) Hypothetical magnetic structure of VI_3 (vanadium and iodine atoms are in blue and orange, respectively). The spin orientations are represented with red arrows or by a + sign indicating that the spins are pointing orthogonally to the view. (c) Comparison of the 60, 40, and 9 K neutron diffraction pattern in the $[0.7 \text{ \AA}^{-1}; 3.3 \text{ \AA}^{-1}]$ Q range. (d) Zoom in the $[1.7 \text{ \AA}^{-1}; 2.05 \text{ \AA}^{-1}]$ Q range to highlight the magnetic contribution to the (110) reflection [with (hkl) indices referring to the $R\bar{3}$ hexagonal cell].

magnetic moment of maximum $0.2 \mu_B$, which is tenfold smaller than expected for V^{3+} ($2 \mu_B$, $S = 1$ for V^{3+}) and is of the order of magnitude of the standard deviation obtained on the Rietveld refinement. Such an observation indicates that the macroscopic ferromagnetic ordering along [001] evidenced by magnetic susceptibility on single crystals [5] does not translate into a long-range complete ordering. This almost-undistinguishable ordered moment may arise from a reduced coherence length in the magnetic structure, which may be due to the presence of defects in the vanadium honeycomb pattern, stacking faults, and weakness of the magnetic interactions across the van der Waals gap. Still, this is not supported by our neutron data since no signs of diffuse magnetic scattering in the patterns are observed at low scattering angles. The existence of an ordered magnetic structure can therefore be questioned, and the small increase in the (110) reflection could just be due to another origin. The apparent contradiction with the macroscopic magnetic measurements that clearly indicates a ferromagnetic behavior still needs to be clarified, and a field-induced ferromagnetic ordering should be further explored as the origin for this contradiction.

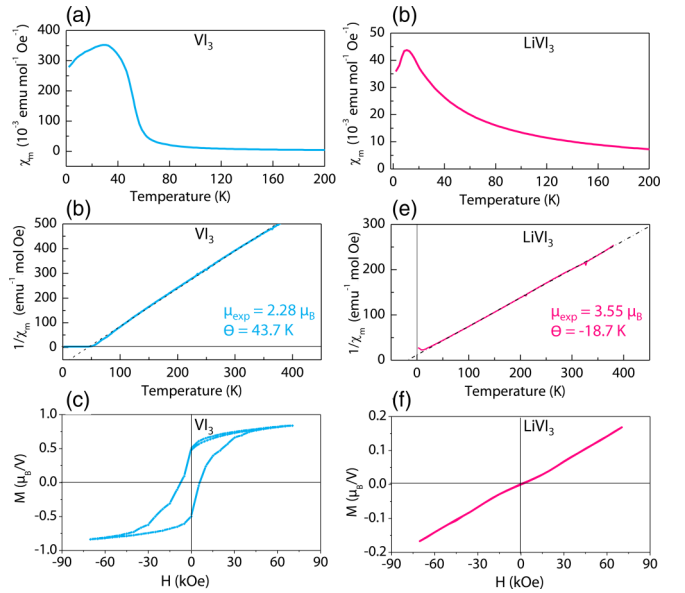


FIG. 9. Temperature dependence of the magnetic susceptibility χ of VI_3 (a), and LiVI_3 (d). Temperature dependence of the inverse of the magnetic susceptibility $1/\chi$ of VI_3 (b) and LiVI_3 (e), measured in zero field cooled (ZFC) conditions. The curves follow at high temperature an ideal Curie-Weiss behavior represented by the dashed line (Curie-Weiss fit). Magnetization curve of VI_3 (c) and LiVI_3 (f) as a function of the applied field measured at 2 K.

C. Magnetic structure and properties of LiVI_3

The magnetic properties of 2D vdW magnets have proven to strongly depend on a plethora of parameters such as electrostatic doping [21], external pressure [22], or layer stacking sequence [23]; hence there is an impetus to explore means of varying T_c in VI_3 . Recently, our group succeeded in inserting lithium atoms inside VI_3 , by means of chemical reducing agents, to form a unique LiVI_3 phase. This compound adopts a structure related to the one of VI_3 [$R\bar{3}$, $a = 7.1442(2) \text{ \AA}$, $c = 20.6666(2) \text{ \AA}$] [10] but it differs in terms of electronic structure by containing one extra valence electron. Consequently, it constitutes an ideal playground to explore the electronic-magnetic relationship in 2D layered iodides.

Magnetic susceptibility measurements were performed on LiVI_3 from 2 to 400 K [Fig. 9(d)] and on VI_3 for the sake of comparison. First, in line with precedent investigations on VI_3 [5–8] a ferromagnetic order at around 50 K was found [cf. Fig. 9(a)]. The linear fit of the high-temperature part of the susceptibility with a Curie-Weiss law indicates an effective moment of $2.28 \mu_B$ per vanadium atom, slightly lower than the one expected for the spin configuration of V^{3+} ($2.83 \mu_B$) and a Weiss temperature of $+43.7 \text{ K}$ [cf. Fig. 9(b)] suggesting predominant ferromagnetic interactions. Moreover, magnetization curves were collected at 2 K in a $[-70 \text{ kOe}; 70 \text{ kOe}]$ range and demonstrate a clear hysteresis loop accounting for a 10 kOe coercive field [cf. Fig. 9(c)], which confirmed the ferromagnetism in VI_3 . On the contrary, LiVI_3 shows an antiferromagnetic order below $T_N = 12 \text{ K}$ with a Curie Weiss temperature $\theta = -18.7 \text{ K}$ and an effective moment of $3.55 \mu_B$ per vanadium, (i.e., a value a bit lower than the $3.87 \mu_B$ expected for a V^{2+} atom). To shed light

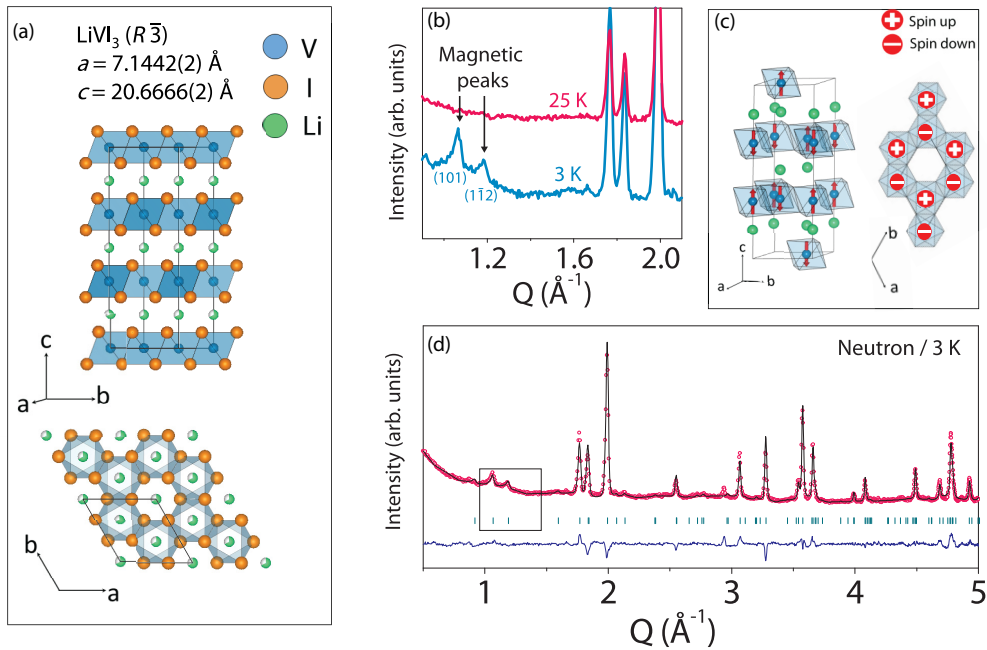


FIG. 10. (a) Structure of LiVI_3 at 300 K. (b) Neutron powder diffraction patterns of LiVI_3 at 25 and 3 K. (c) magnetic structure of LiVI_3 spin orientations are represented with red arrows, the right panel represents the spin organization in a single layer. (d) Rietveld refinements of LiVI_3 at 3 K ($\lambda = 2.4395 \text{ \AA}$). The pink circles, black continuous line, and bottom blue line represent the observed, calculated, and difference patterns, respectively. Vertical green tick bars indicate the Bragg positions.

on the magnetic ordering of LiVI_3 , both synchrotron x-ray and neutron diffraction experiments were performed at low temperature. The refinement of the SXR pattern of LiVI_3 at 10 K (cf. Fig. S7 [18]) indicates that the RT structure is preserved with solely a contraction of the lattice parameters. Lastly, neutron diffraction patterns collected between 25 and 3 K show the emergence of extra magnetic peaks at low angle [cf. Fig. 10(b)].

Altogether, these observations, combined with the magnetic behavior described above, suggest the formation of a long-range magnetic structure at low temperature. Further exploiting the NPD patterns, we could index the extra reflections using a $\mathbf{k} = (0, 0, 0)$ propagation vector and determine the associated magnetic structure using the ISODISTORT program [24,25]. The 3 K neutron diffraction pattern was successfully refined in the $R\bar{3}^7$ magnetic space group (cf. Fig. 10(d) and Table S7 [18]), where all the magnetic moments are found to be oriented in the [001] direction with both intra- and inter-layer adjacent vanadium atoms being antiferromagnetically coupled [cf. Fig. 10(c)]. Surprisingly, the refined magnetic moment was found to be equal to $1.68(6) \mu_B$, i.e., lower than the expected $3 \mu_B$ value for a d^3 ion. Such a difference could arise from a reduced coherence length induced by a defect such as stacking faults and weakness of interlayer interaction.

Understanding this Li-driven ferromagnetic to antiferromagnetic transition calls for a comparison of both VI_3 and LiVI_3 in terms of crystal and electronic structures. Firstly, the redox state of vanadium changes from $\text{V}^{3+}(d^2)$ to $\text{V}^{2+}(d^3)$ leading to half-filled t_{2g} electronic states, i.e., similarly to that of ferromagnetic CrI_3 . Besides, although CrI_3 and LiVI_3 share exactly the same $R\bar{3}$ structure at low temperature, they

differ by longer M -I bond lengths as well as larger inter-layer distances ($\text{V-I} = 2.90 \text{ \AA}$, interlayer = 6.84 \AA , at 100 K) for LiVI_3 as compared to CrI_3 ($\text{Cr-I} = 2.73 \text{ \AA}$, interlayer = 6.60 \AA , at 90 K). Moreover, it is worth remembering that several first-principle calculation investigations [23,26] on bulk CrI_3 revealed a strong intralayer ferromagnetic exchange as opposed to a weaker ferromagnetic interlayer coupling. Thus, presently, the increase of the interlayer and M - M distances (where M stands for transition metal) from CrI_3 to LiVI_3 may change the competing nature of the interlayer and intralayer couplings and consequently explain the antiferromagnetic interaction observed for LiVI_3 . However, further theoretical investigations are needed to support our explanation and to better understand how the intra vs inter- M - M distance variation impacts the magnetic properties of layered van der Waals materials.

III. CONCLUSION

We report here an extensive investigation of the VI_3 structural evolution at low temperature using both synchrotron x-ray and neutron powder diffraction. We confirm that the room-temperature $R\bar{3}$ VI_3 phase undergoes two structural transitions upon cooling at 76 and 32 K together with a ferromagnetic ordering at 50 K. Moreover, we provide a structural model of this compound in the whole temperature range and demonstrate that the 76 and 32 K phase transitions are solely due to distortion of the vanadium honeycomb networks with minute changes of the V-V distances. Additionally, we show by neutron diffraction that the magnetic moments below T_c are extremely reduced from the expected for long-range ordered V^{2+} . We extended our study to the recently reported LiVI_3

layered phase and reveal the presence of an antiferromagnetic order at $T_N = 12$ K in contrast to the isostructural and electronic equivalent CrI_3 ferromagnetic phase. We rationalize this finding that is nested in a delicate balance between the interlayer and/or the M - M distances within these materials. In this context, our work could stimulate future research on finding other van der Waals ferromagnets within the halide family and beyond, hence enabling a deeper understanding of these compounds.

ACKNOWLEDGMENTS

Beam time on MSPD at ALBA was granted through in-house Proposal No. 2021024879. T.M. acknowledges the Ecole Normale Supérieure Paris-Saclay for funding through his Ph.D. scholarship. N.D. acknowledges the Ecole Normale Supérieure for funding through his Ph.D. Scholarship. The authors acknowledge the staff of the MPBT (physical properties—low temperature) platform of Sorbonne Université for their support.

- [1] R. Mas-Ballesté, C. Gómez-Navarro, J. Gómez-Herrero, and F. Zamora, 2D materials: To graphene and beyond, *Nanoscale* **3**, 20 (2011).
- [2] N. D. Mermin and H. Wagner, Absence of Ferromagnetism or Antiferromagnetism in One- or Two-Dimensional Isotropic Heisenberg Models, *Phys. Rev. Lett.* **17**, 1133 (1966).
- [3] C. Gong, L. Li, Z. Li, H. Ji, A. Stern, Y. Xia, T. Cao, W. Bao, C. Wang, Y. Wang, Z. Q. Qiu, R. J. Cava, S. G. Louie, J. Xia, and X. Zhang, Discovery of intrinsic ferromagnetism in two-dimensional van der Waals crystals, *Nature* **546**, 265 (2017).
- [4] M. A. McGuire, H. Dixit, V. R. Cooper, and B. C. Sales, Coupling of crystal structure and magnetism in the layered, ferromagnetic insulator CrI_3 , *Chem. Mater.* **27**, 612 (2015).
- [5] T. Kong, K. Stolze, E. I. Timmons, J. Tao, D. Ni, S. Guo, Z. Yang, R. Prozorov, and R. J. Cava, VI_3 —a new layered ferromagnetic semiconductor, *Adv. Mater.* **31**, 1808074 (2019).
- [6] S. Tian, J. F. Zhang, C. Li, T. Ying, S. Li, X. Zhang, K. Liu, and H. Lei, Ferromagnetic van der Waals crystal VI_3 , *J. Am. Chem. Soc.* **141**, 5326 (2019).
- [7] S. Son, M. J. Coak, N. Lee, J. Kim, T. Y. Kim, H. Hamidov, H. Cho, C. Liu, D. M. Jarvis, P. A. C. Brown, J. H. Kim, C. H. Park, D. I. Khomskii, S. S. Saxena, and J. G. Park, Bulk properties of the van der Waals hard ferromagnet VI_3 , *Phys. Rev. B* **99**, 041402(R) (2019).
- [8] P. Doležal, M. Kratochvílová, V. Holý, P. Čermák, V. Sechovský, M. Dušek, M. Míšek, T. Chakraborty, Y. Noda, S. Son, and J.-G. Park, Crystal structures and phase transitions of the van der Waals ferromagnet VI_3 , *Phys. Rev. Materials* **3**, 121401(R) (2019).
- [9] E. Gati, Y. Inagaki, T. Kong, R. J. Cava, Y. Furukawa, P. C. Canfield, and S. L. Bud'ko, Multiple ferromagnetic transitions and structural distortion in the van der Waals ferromagnet VI_3 at ambient and finite pressures, *Phys. Rev. B* **100**, 094408 (2019).
- [10] N. Dubouis, T. Marchandier, G. Rouse, F. Marchini, F. Fauth, M. Avdeev, A. Iadecola, B. Porcheron, M. Deschamps, J.-M. Tarascon, and A. Grimaud, Superconcentrated electrolytes widens insertion electrochemistry to soluble layered halides, ChemRxiv (unpublished).
- [11] F. Fauth, I. Peral, C. Popescu, and M. Knapp, The new material science powder diffraction beamline at ALBA synchrotron, *Powder Diffr.* **28**, S360 (2013).
- [12] F. Fauth, R. Boer, F. Gil-Ortiz, C. Popescu, O. Vallcorba, I. Peral, D. Fullà, J. Benach, and J. Juanhuix, The crystallography stations at the ALBA synchrotron, *Eur. Phys. J. Plus* **130**, 160 (2015).
- [13] P. J. E. M. Van Der Linden, M. Moretti Sala, C. Henriquet, M. Rossi, K. Ohgushi, F. Fauth, L. Simonelli, C. Marini, E. Fraga, C. Murray, J. Potter, and M. Krisch, A compact and versatile dynamic flow cryostat for photon science, *Rev. Sci. Instrum.* **87**, 115103 (2016).
- [14] M. Avdeev and J. R. Hester, ECHIDNA: A decade of high-resolution neutron powder diffraction at OPAL, *J. Appl. Crystallogr.* **51**, 1597 (2018).
- [15] A. J. Studer, M. E. Hagen, and T. J. Noakes, Wombat: The high-intensity powder diffractometer at the OPAL reactor, *Physica B: Condensed Matter* **385-386**, 1013 (2006).
- [16] J. Rodríguez-Carvajal, Recent advances in magnetic structure determination by neutron powder diffraction, *Phys. B (Amsterdam, Neth.)* **192**, 55 (1993).
- [17] D. Juza, D. Giegling, and H. Schäfer, Über die vanadinjodide VJ_2 und VJ_3 , *Z. Anorg. Allg. Chem.* **366**, 121 (1969).
- [18] See Supplemental Material at <http://link.aps.org/supplemental/10.1103/PhysRevB.104.014105> for additional Rietveld refinements, crystallographic tables, structure transformation details, and structure files (.cif).
- [19] B. M. De Boisse, M. Reynaud, J. Ma, J. Kikkawa, S. Nishimura, M. Casas-Cabanas, C. Delmas, M. Okubo, and A. Yamada, Coulombic self-ordering upon charging a large-capacity layered cathode material for rechargeable batteries, *Nat. Commun.* **10**, 2185 (2019).
- [20] M. A. McGuire, Crystal and magnetic structures in layered, transition metal dihalides and trihalides, *Crystals* **7**, 121 (2017).
- [21] S. Jiang, L. Li, Z. Wang, K. F. Mak, and J. Shan, Controlling magnetism in 2D CrI_3 by electrostatic doping, *Nat. Nanotechnol.* **13**, 549 (2018).
- [22] T. Li, S. Jiang, N. Sivadas, Z. Wang, Y. Xu, D. Weber, J. E. Goldberger, K. Watanabe, T. Taniguchi, C. J. Fennie, K. F. Mak, and J. Shan, Pressure-controlled interlayer magnetism in atomically thin CrI_3 , *Nat. Mater.* **18**, 1303 (2019).
- [23] N. Sivadas, S. Okamoto, X. Xu, C. J. Fennie, and D. Xiao, Stacking-dependent magnetism in bilayer CrI_3 , *Nano Lett.* **18**, 7658 (2018).
- [24] H. T. Stokes, D. M. Hatch, and B. J. Campbell, ISODISTORT, ISOTROPY Software Suite; iso.byu.edu.
- [25] B. J. Campbell, H. T. Stokes, D. E. Tanner, and D. M. Hatch, ISODISPLACE: A web-based tool for exploring structural distortions, *J. Appl. Crystallogr.* **39**, 607 (2006).
- [26] P. Jiang, C. Wang, D. Chen, Z. Zhong, Z. Yuan, Z. Y. Lu, and W. Ji, Stacking tunable interlayer magnetism in bilayer CrI_3 , *Phys. Rev. B* **99**, 144401 (2019).